

Supplementary Data: Effect of leading-edge curvature actuation on flapping fin performance

David Fernández-Gutiérrez¹ and Wim M. van Rees^{1†}

¹Department of Mechanical Engineering, Massachusetts Institute of Technology, Cambridge, MA 02139, USA

Appendix A. Verification of 3D Navier-Stokes solver

To evaluate the validity of the numerical scheme for a flapping fin simulation specifically, we investigate the flow around an ellipsoid heaving and pitching around its centroid, and compare our force coefficient results to those presented in [Dong *et al.* \(2006\)](#). Rather than representing the ellipsoid directly through its continuum geometric description, we use our algorithm as described in the main text to describe the shape. Specifically, twenty-one rays are distributed along the ellipsoid height such that

$$v_i = 0.5 \cos\left(\pi \frac{N_r - i}{N_r - 1}\right), \quad i = 1..N_r. \quad (\text{A1})$$

The aspect ratio of the ellipse is $a_z/a_x = 4$, where a_x and a_z are the ellipsoid length and height, respectively. We adopt the same configuration as [Dong *et al.* \(2006\)](#) by setting $Re = U_\infty a_x / \nu = 200$, $St = 0.3$, $\tilde{A}_y = 0.5$, $A_\theta = 30^\circ$, and $\varphi_\theta = -90^\circ$.

Figure [A.1](#) compares the reported time-history of thrust coefficients with the values from our computational model. We include the time-series obtained with various grid resolutions, compared with the data taken from the reference paper.

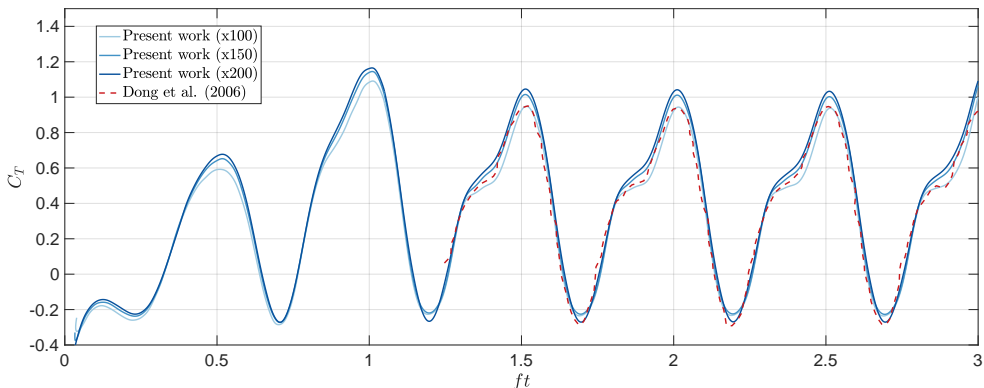


FIGURE A.1. Comparison between our results (*solid*) and the results adapted from [Dong *et al.* \(2006\)](#) (*red dashed*) of the thrust coefficient time-series for a heaving and pitching ellipsoid with aspect ratio $a_z/a_x = 4$.

We obtain a very similar match, although some differences appear in peak amplitude. Our computed forces are, however, converged, as shown by the grid resolution study in [appendix C.2](#). Together with the previous validations of the methodology ([Gazzola *et al.* 2011](#)), this validation case provides further confidence in our results.

† Email address for correspondence: wvanrees@mit.edu

Appendix B. Curvature parametrization

We provide in this appendix further details of our choice to parametrize the normal curvature, stated in equation (3.5) in the main text. Below, we discuss our choice for the zero phase-shift between chordwise curvature and the heaving motion, the 90° phase-shift between chordwise and spanwise curvature, and the $\cos \beta(v)$ correction factor in the chordwise curvature term. Finally, we show three-dimensional snapshots of the curving fin with different parameter combinations to accompany figure 2 of the main text.

B.1. Description of chordwise curvature variations

To provide some context on our choice of zero phase-shift between chordwise curvature and heaving/pitching motion, we reproduce in figure B.1 below a series of snapshots from experimental observations of Esposito *et al.* (2012). We combine that with a fin with chordwise curvature variations chosen in-phase with the heave and, in this case, a negative chordwise curvature coefficient. The comparison demonstrates that our choice of phase-shift, as well as our choice of constant normal curvature, can be used as a first-order approximation to the motion pattern of the fish. We do not exclude that other natural swimmers and/or other swimming conditions would lead to different fin deformation patterns, nor that different phase-shifts between heave and chordwise curvature would improve performance over what we have seen; however, we leave that for future work.

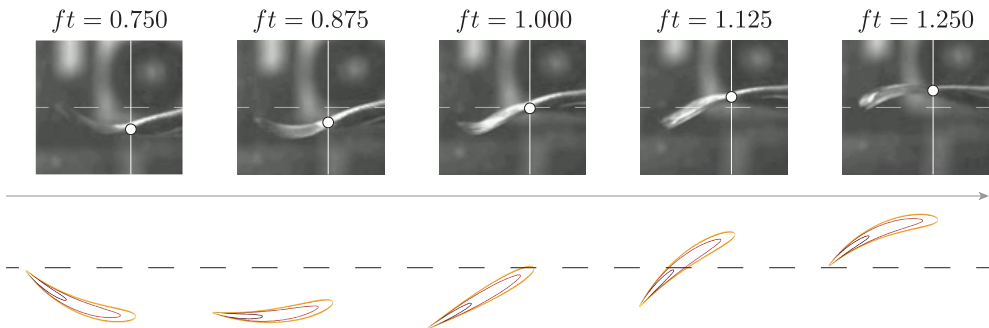


FIGURE B.1. Comparison of experimental results adapted from Esposito *et al.* (2012) (*top*) with horizontal cross-sections taken at $z/C = \{0.000, 0.175, 0.350, 0.525\}$ (*bottom*) obtained using our curvature parametrization with $a_c = -0.8$ and $a_s = 0.0$. White dots identify the estimated location of the fin LE in the experimental observations.

B.2. Description of spanwise curvature variations

We have represented the spanwise curvature in equation (3.5) through an additive term proportional to v^2 , and with a 90° phase-shift compared with the chordwise curvature. An alternative approach was adopted in (Esposito *et al.* 2012), where the cupping mode is characterized by a phase difference between the outer and middle rays.

In our notation, combining chordwise curvature variations with a top/bottom symmetric spanwise varying phase shift would be defined by $\kappa_0^n(v, t) = a_c \sin(2\pi ft + \tilde{a}_s v^2)$, with a_c and \tilde{a}_s the chordwise and spanwise curvature parameters, respectively. Expanding this expression in the spanwise phase shift $\tilde{a}_s v^2$ gives $\kappa_0^n(v, t) = a_c \sin(2\pi ft) + a_c \tilde{a}_s v^2 \cos(2\pi ft) + \mathcal{O}((\tilde{a}_s v^2)^2)$. For small spanwise curvature variations we can recover our profile by replacing $a_c \tilde{a}_s$ with a_s as an independent parameter.

The perspective of spanwise curvature variations through a spanwise varying phase

shift thus leads to approximately the same geometry as our parametrization, at least for small spanwise curvature variations and non-zero chordwise curvature variations. On the other hand, our parametrization enables us to independently vary chordwise and spanwise curvature amplitudes using only two parameters. As written above, more elaborate, higher-dimensional parametrizations of both chordwise and spanwise curvature are left for future work.

B.3. Correction factor on chordwise curvature variations

We intend the chordwise curvature parameter a_c to determine only the cross-section of the mid-surface in any $x - y$ plane cut. Under the assumption of uniform κ^n along each ray adopted in this work, this cross-section follows a circular trajectory \dagger . This implies that the deformed mid-surface must be embedded on a cylinder of radius C/a_c as shown in figure B.2, where a_c is the coefficient modulating the non-dimensional chordwise curvature (section 3.2). We show here that when the ray angle $\beta \neq 0$, this shape cannot be generated with constant κ^n across rays, leading to the correction factor $\cos \beta(v)$ in equation (3.5) of the main text.

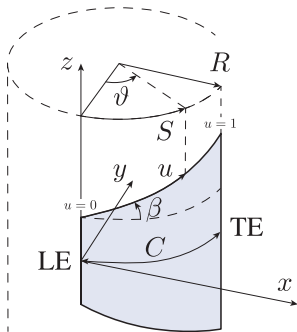


FIGURE B.2. The fin shape (in blue) follows the surface of a cylinder with radius C/a_c in a sole chordwise curvature configuration as determined by a_c .

Starting from equations (2.3)-(2.4), we recall that the ray shape is reconstructed starting from the LE through integration along its chord. The LE is aligned with the z -axis, and, consistent with the rest of this work, we consider the case where the TE is also described by a straight line parallel to the z -axis.

Denoting ϑ as the angular coordinate over the cylinder containing the mid-surface, as shown in figure B.2, we can establish the following geometrical relation:

$$\vartheta = \frac{S}{R} = \frac{u c(v) \cos \beta(v)}{C/a_c} = u a_c, \quad (\text{B1})$$

since, for a cylindrical deformation of a fin with straight TE, we can directly write $C = c(v) \cos \beta(v)$. Using the definition of a cylindrical surface, we can determine the desired tangent and normal vectors for any ray at inclination angle $\beta(v)$ as

$$\hat{\mathbf{t}} = \cos(\beta) \cos(\vartheta) \hat{\mathbf{x}} + \cos(\beta) \sin(\vartheta) \hat{\mathbf{y}} + \sin(\beta) \hat{\mathbf{z}}, \quad (\text{B2})$$

$$\hat{\mathbf{n}} = -\sin(\vartheta) \hat{\mathbf{x}} + \cos(\vartheta) \hat{\mathbf{y}}. \quad (\text{B3})$$

\dagger Note that the deformed cross-section remains at the $x - y$ plane since there is no spanwise curvature, so $\kappa^t(u, v = 0, t) = \kappa^g(u, v = 0, t) = 0$

From this, we can determine analytically the non-dimensional normal curvature $\kappa^n(v)$ using its geometrical definition from equation (2.2),

$$\kappa^n = \frac{d\hat{\mathbf{t}}}{du} \cdot \hat{\mathbf{n}} = a_c \cos(\beta), \quad (\text{B } 4)$$

In dimensional form this expression becomes,

$$\frac{\kappa^n}{c(v)} = \frac{a_c}{c(v)} \cos(\beta(v)) = \frac{a_c}{C} \cos^2(\beta(v)), \quad (\text{B } 5)$$

The above derivation demonstrates that for a cylindrical fin deformation, the correction factor $\cos(\beta(v))$ in equation (3.5) is required to account for the particular direction of each ray.

B.4. Visualizations of 3D flapping fins

Figure B.3 shows isometric views of the deformed fin under the same curvature regimes and time-stamps plotted in figure 2 in the manuscript. In addition, Movie 1 provided as part of the supplementary data compares the deformed fin shape during a flapping cycle subject to further combinations of positive, zero, and negative chordwise and spanwise curvature coefficients.

Appendix C. Numerical settings

C.1. Mid-surface area variations

Our algorithm to construct the mid-surface, as presented in section 2.1.2 of the main text, enforces membrane extensibility through the condition $d\mathbf{r}(u, v) \cdot \hat{\mathbf{e}}_v(u, v) = d\mathbf{r}_0(u, v) \cdot \hat{\mathbf{e}}_{v,0}(u, v)$, where $d\mathbf{r}$ and $d\mathbf{r}_0$ are the differentials of the deformed and undeformed mid-surface position, respectively, and $\hat{\mathbf{e}}_v$ and $\hat{\mathbf{e}}_{v,0}$ the unit vectors along the deformed and undeformed mid-surface v -direction. Since the angle between the directions along and across rays over the fin varies as the curvature components change over time, this criterion induces a small change on the actual mid-surface area as the fin deforms. To quantify this, we computed the mid-surface area variation arising from the curvature distribution change over a flapping cycle. The left panel in figure C.1 shows such variations for various curvature regimes covering the range plotted in figure B.3, where $A(t)$ is the time-varying mid-surface area computed as

$$A(t) = \frac{1}{2} \sum_{\substack{i=1 \\ j=1}}^{\substack{i=N_v-1 \\ j=N_u-1}} \left\| (\mathbf{r}_{i,j+1} - \mathbf{r}_{i,j}) \times (\mathbf{r}_{i+1,j+1} - \mathbf{r}_{i,j}) \right\| + \left\| (\mathbf{r}_{i+1,j+1} - \mathbf{r}_{i,j}) \times (\mathbf{r}_{i+1,j} - \mathbf{r}_{i,j}) \right\| \quad (\text{C } 1)$$

and A_0 is the known mid-surface area of the undeformed fin.

The results show a maximum area variation below 0.5% for the largest curvature variations considered in this work. For reference, the right panel of figure C.1 shows the variation in length of the TE, where

$$d_{TE} = \sum_{j=1}^{j=N_u-1} \left\| \mathbf{r}_{N_v,j+1} - \mathbf{r}_{N_v,j} \right\| \quad (\text{C } 2)$$

and d_0 is the known length of the undeformed TE, confirming how the absolute value of this metric remains below the maximum deviation threshold set to $\epsilon^{\text{dist}} = 5 \times 10^{-8}$ in our simulations.

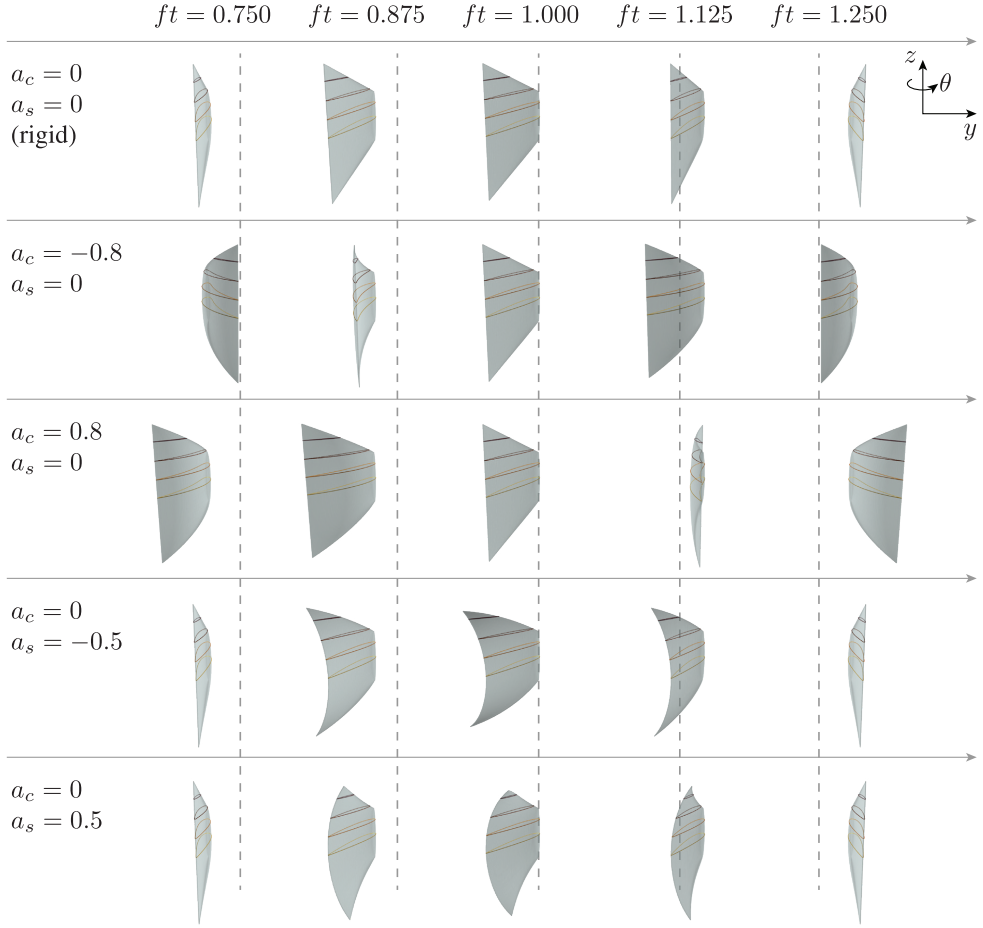


FIGURE B.3. Isometric views of the deformed fin under various curvature regimes obtained within the two-dimensional parametrization (a_c , a_s). Dashed vertical lines identify the $x - z$ plane at each time-step

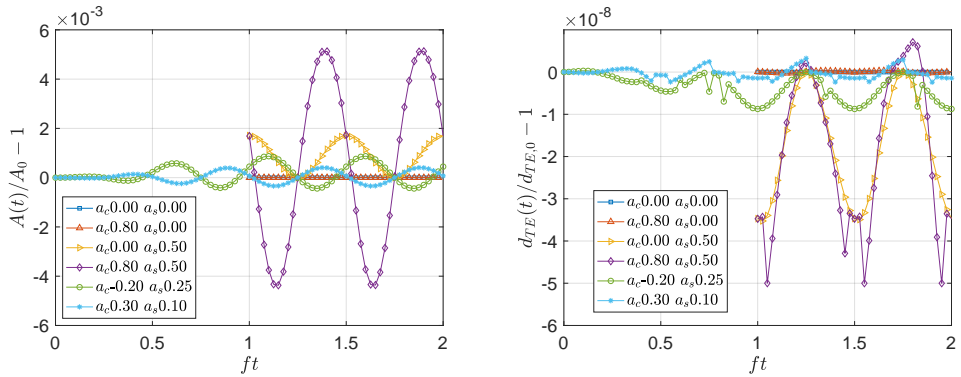


FIGURE C.1. Mid-surface area change (*left*) and TE length change (*right*) over a flapping cycle for various curvature regimes

C.2. Grid convergence

The trapezoidal fin described in section 3 is used here to evaluate the grid convergence of the numerical scheme. In particular, we focus on three characteristic configurations from the range of simulations analyzed in section 4: the rigid fin, the curved fin that yields the largest efficiency ($a_c = -0.2$ and $a_s = 0.25$), and the curved fin that produces the larger thrust ($a_c = 0.3$ and $a_s = 0.1$).

Table 1 summarizes the cycle-averaged thrust and power coefficients computed with four different grid resolutions of 100, 150, 200, and 250 points along C . We include also in table 1 the difference each in metric with respect to the finest resolution, defined for a generic variable ϕ as $\Delta_\phi = |\phi/\phi_{n_x/C=250} - 1|$. In addition, figure C.2 shows the convergence of time-series of thrust and power coefficients computed with each grid resolution for the configuration generating the maximum thrust, which yields the largest flow perturbations.

n_x/C	rigid: $a_c = 0, a_s = 0$		max. thrust: $a_c = 0.3, a_s = 0.1$		max. efficiency: $a_c = -0.2, a_s = 0.25$	
	$\overline{C_T}$	Δ_{C_T}	$\overline{C_P}$	Δ_{C_P}	$\overline{C_T}$	Δ_{C_T}
100	0.122	28.7%	0.832	0.7%	0.140	29.6%
150	0.151	12.0%	0.829	0.3%	0.174	12.7%
200	0.164	4.3%	0.827	0.1%	0.189	4.8%
250	0.172	-	0.827	-	0.199	-

TABLE 1. Thrust and power coefficient variation with grid resolution. We report both the values of thrust and power coefficient for each case, as well as the difference with respect to the finest resolution simulated.

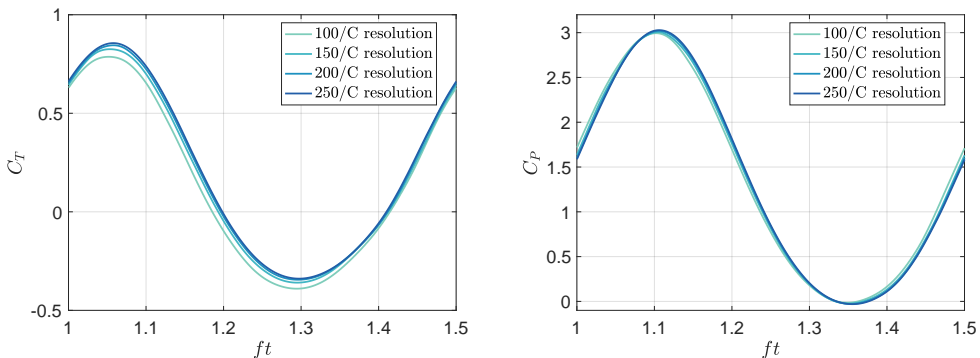


FIGURE C.2. Thrust (left) and power (right) coefficients of the fin with various grid resolutions for the maximum thrust conditions ($a_c = 0.3$ and $a_s = 0.1$).

The results show that the power coefficient is very robust to the resolution, both in terms of its time evolution as well as the time average. The time evolution of the thrust coefficient is also converging well within this resolution range, but the average value of a cycle is still sensitive to resolution changes. Based on this data, we have chosen to use 200 elements per chord as a balance between computational speed and accuracy. We emphasize that we are specifically interested in the effect of the different parameters, and the data in this section shows that this resolution is sufficient to predict trends in parameter variations, as well as a sufficiently close quantitative estimate of the metrics. The fact that the power coefficient is especially insensitive to the resolution further

gives us confidence that our computed efficiency, defined as $\eta = \overline{C_T}/\overline{C_P}$, also provides sufficiently accuracy to support the results of this work.

C.3. Initialization and measurement window

To justify our choice to measure the force and power coefficients in the third half-cycle after initialization, we simulated the rigid fin, the maximum thrust fin, and the maximum efficiency fins, up to $ft = 2.0$. We then plot the relative difference in thrust and power coefficients when averaged between ft_0 and $ft_0 + 0.5$ as a function of ft_0 , made non-dimensional with the result at $ft_0 = 1.5$, *i.e.* the last half-cycle available. Figures C.3-C.4 show that choosing $ft_0 = 1.0$, as we have, leads to around 1% error in the thrust coefficient for the maximum thrust case, and around 0.5% error for the power coefficient of all three cases. Compared with the differences in hydrodynamic coefficients we discuss in the manuscript, we deem this accuracy acceptable to base our conclusions on.

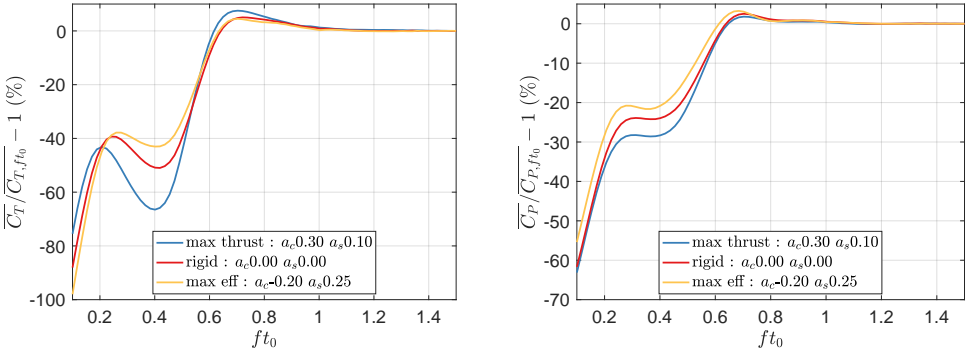


FIGURE C.3. Half-cycle averaged thrust (*left*) and power (*right*) coefficients of the fin as a function of the averaging start time ft_0

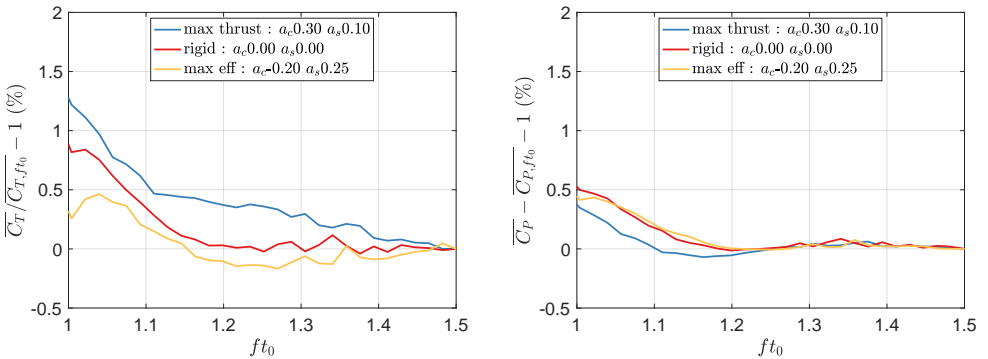


FIGURE C.4. Variation of the half-cycle averaged thrust (*left*) and power (*right*) coefficients of the fin between $ft_0 = 1.0$ and $ft_0 = 1.5$

Appendix D. Effect of chordwise curvature parameter a_c

D.1. Effect of pitch kinematics variations on rigid fin performance

Figure D.1 shows the effect of changing the pitch amplitude (top) or the pitch phase (bottom) on the thrust and power coefficients, and the efficiency (left-to-right). In all cases the fin undergoes harmonic heave and pitch motions without curvature deformations.

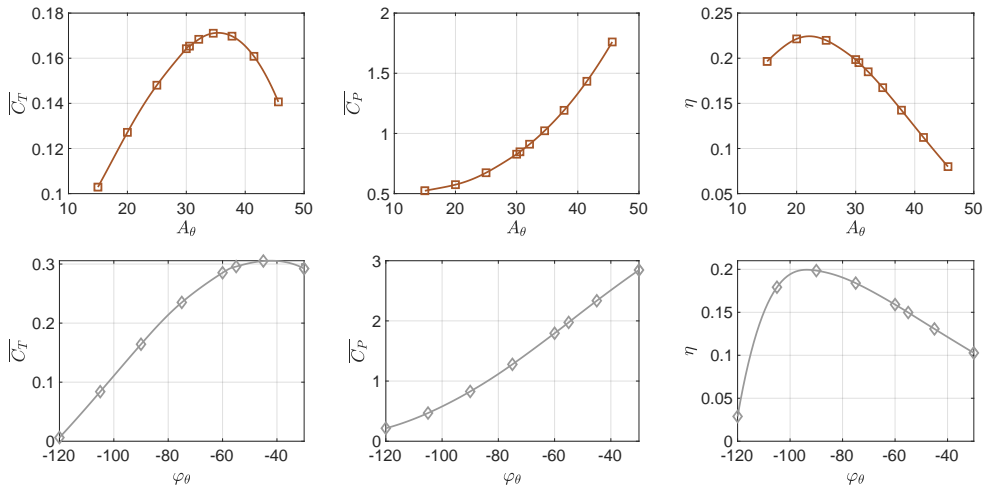


FIGURE D.1. Cycle-averaged thrust coefficient (*left*), power coefficient (*center*), and efficiency (*right*) of the rigid fin as a function of the pitch angle amplitude (*top*) and phase angle with respect to heave (*bottom*).

D.2. Thrust and lift coefficient time series

Figure D.2 shows the time evolution of thrust (left) and lift (right) coefficients for the rigid fin (in red), the fin with curvature variations $a_c = 0.8$ and $a_s = 0$ (in blue), and the κ -pitch configuration with $a_c = 0.8$ (in yellow).

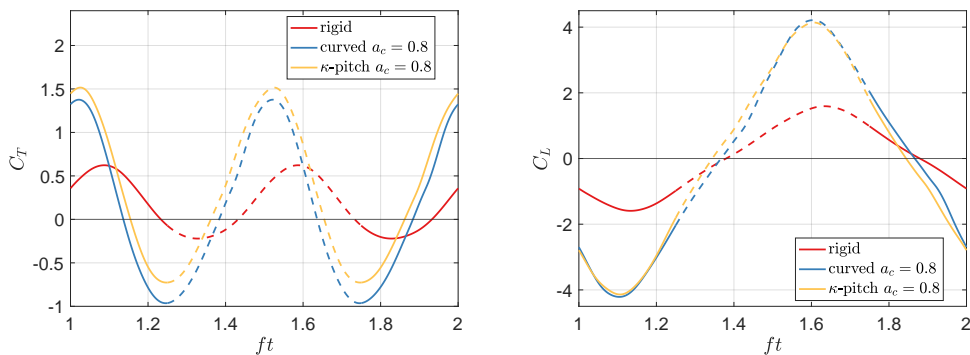


FIGURE D.2. Thrust (*left*) and lift (*right*) coefficients variation during a flapping cycle of the rigid, curved, and κ -pitch configurations with $a_c = 0.8$. Solid and dashed lines identify the upstroke and downstroke half-cycles, respectively.

Appendix E. Robustness of results to Strouhal number and planform changes

E.1. Strouhal number

To evaluate the influence of the flapping frequency on the results, we have conducted additional simulations with a higher Strouhal number, $St = 0.6$, varying only the chordwise curvature amplitude as the dominant parameter. Figure E.1 shows the cycle-averaged thrust and power coefficients and efficiency obtained. Consistent with the observations of Buchholz & Smits (2008), a higher Strouhal number augments the magnitude of the thrust and power coefficients of the rigid fin, and the fin operates at slightly decreased efficiency. For a qualitative comparison of the effect of chordwise curvature variations, figure E.2 shows the same data, but we normalized each curve with their respective value of the rigid fin ($a_c = 0$). The plots show that the qualitative trends of chordwise curvature we described in the main text still hold at $St = 0.6$: for $a_c < 0$ the thrust decreases and efficiency increases, whereas for $a_c > 0$ the trends are reversed. We further observe an interesting scaling behavior where the relative increases in thrust and efficiency, respectively, are much larger at $St = 0.6$ compared with $St = 0.3$, and happen at larger absolute curvature coefficients. Exploring these effects is left for future work.

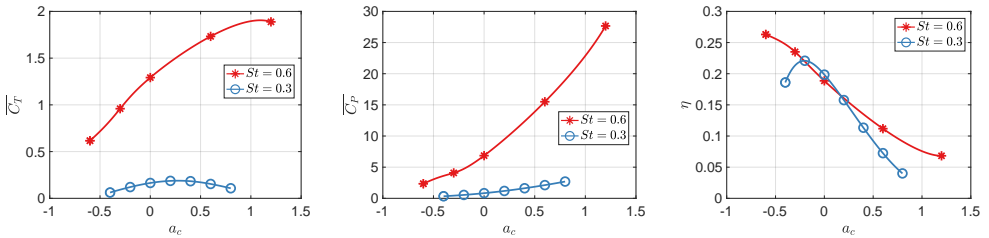


FIGURE E.1. Cycle-averaged thrust (*left*) and power (*center*) coefficients and efficiency (*right*) results as a function of the chordwise curvature amplitude a_c for the curved fin with $St = 0.3$ and $St = 0.6$

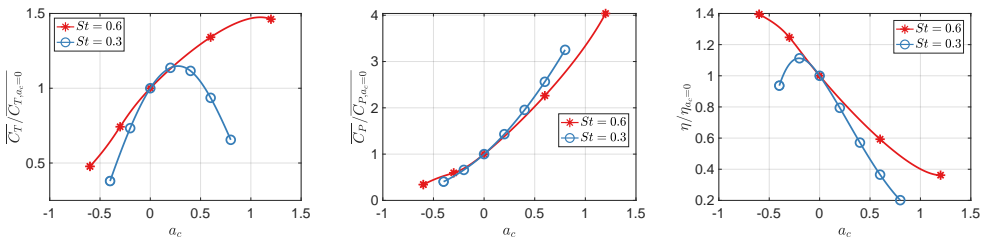


FIGURE E.2. Cycle-averaged thrust (*left*) and power (*center*) coefficients and efficiency (*right*) relative to the undeformed fin values ($a_c = 0$) for the curved fin with $St = 0.3$ and $St = 0.6$

E.2. Square fin planform and 2D results

Here we explore robustness of our results from the main text to two drastic geometry changes: the change of our trapezoidal planform shape to a square planform shape, and the change of our finite aspect ratio to an infinite aspect ratio, where the latter effect is achieved using 2D simulations.

The square planform is defined by setting $\beta(v) = 0$ and $H = C$, with all other settings

kept as in the main text. The effect of varying a_c and a_s are displayed in figure E.3, and selected flow visualizations are shown in figure E.4. We observe that the same trends of the trapezoidal fin are retained, with a small decrease in the cycle-averaged thrust magnitudes of the square fin.

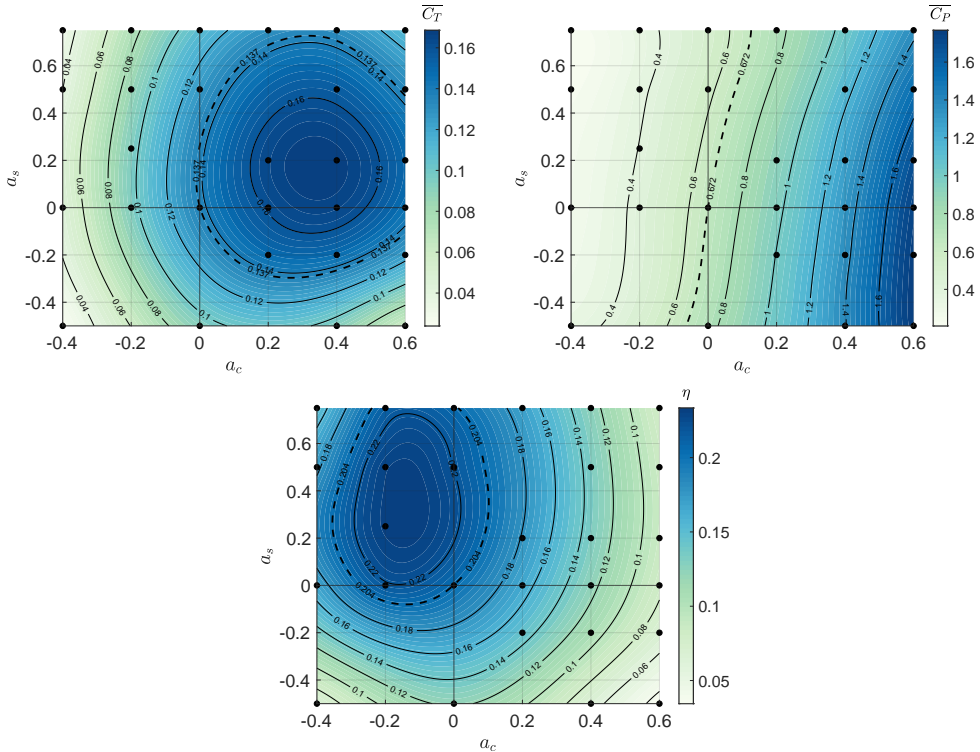


FIGURE E.3. Cycle-averaged thrust (*top-left*) and power (*top-right*) coefficients and efficiency (*bottom*) results from Navier-Stokes simulations of a square fin (*black dots*), and an interpolated contour plot based on these results, as a function of the two curvature parameters a_c and a_s .

The isolated effect of chordwise curvature coefficient is compared in figure E.5 between the trapezoidal planform, a square planform, and a 2D fin. The 2D results are generated with the same numerical algorithm and settings as the 3D results, using the code described in (Rossinelli *et al.* 2015). The results are striking in their qualitative consistency, demonstrating that the effect of chordwise curvature variations is largely independent of fin planform and aspect ratio.

rigid

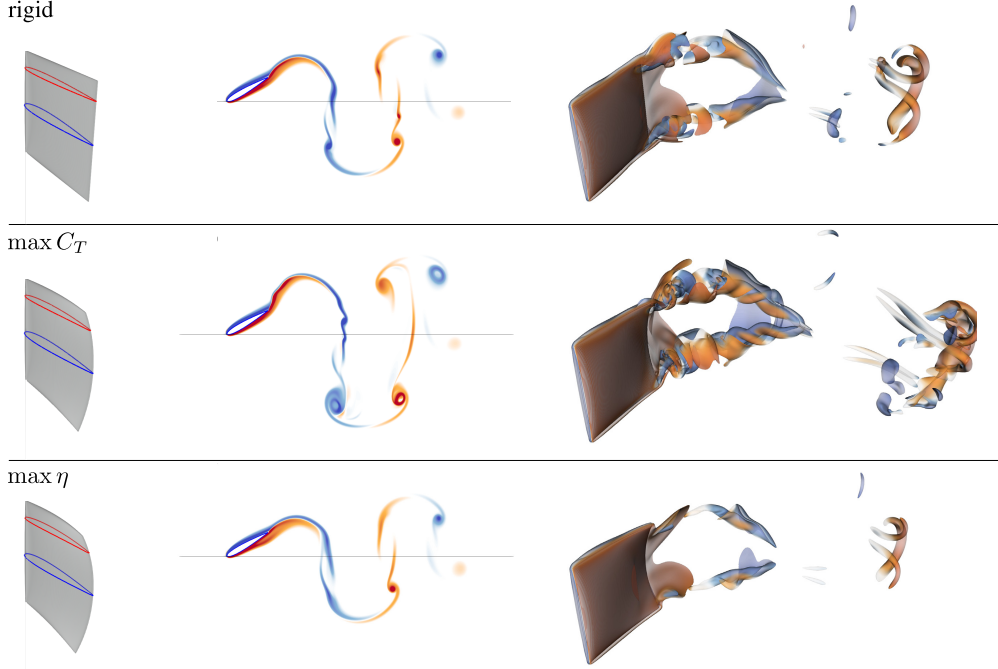


FIGURE E.4. Square fin shape (*left*), ω_z vorticity field at $v = 0$ (*middle*), and 3D vorticity field (*right*) for the rigid configuration (*top*, $a_c = 0.0$, $a_s = 0.0$), the maximum computed thrust configuration (*middle*, $a_c = 0.4$, $a_s = 0.2$), and the maximum computed efficiency configuration (*bottom*, $a_c = -0.2$, $a_s = 0.25$), all at $ft = 1.5$. The 3D flow structures are visualized using vorticity magnitude, and both 2D and 3D visualizations are colored by ω_z .

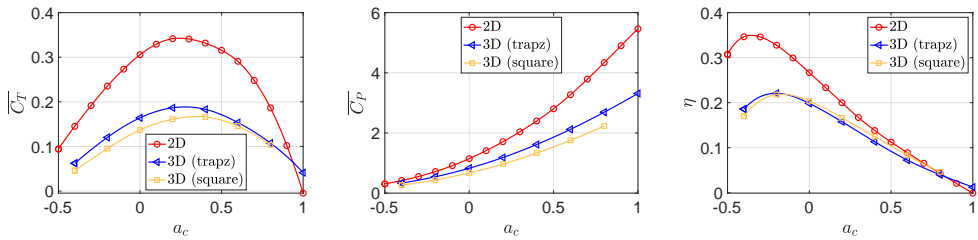


FIGURE E.5. Cycle-averaged thrust coefficient (*left*), power coefficient (*center*), and efficiency (*right*) of the 2D, trapezoidal, and square fins as a function of the chordwise curvature amplitude a_c , with $a_s = 0$ for the 3D trapezoidal and square fins.

REFERENCES

- BUCHHOLZ, JAMES H.J. & SMITS, ALEXANDER J. 2008 The wake structure and thrust performance of a rigid low-aspect-ratio pitching panel. *Journal of Fluid Mechanics* **603**, 331–365.
- DONG, H., MITTAL, R. & NAJJAR, F. M. 2006 Wake topology and hydrodynamic performance of low-aspect-ratio flapping foils. *Journal of Fluid Mechanics* **566**, 309–343.
- ESPOSITO, CHRISTOPHER J., TANGORRA, JAMES L., FLAMMANG, BROOKE E. & LAUDER, GEORGE V. 2012 A robotic fish caudal fin: effects of stiffness and motor program on locomotor performance. *Journal of Experimental Biology* **215** (1), 56–67.
- GAZZOLA, MATTIA, CHATELAIN, PHILIPPE, VAN REES, WIM M. & KOUMOUTSAKOS, PETROS 2011 Simulations of single and multiple swimmers with non-divergence free deforming geometries. *J. of Computational Physics* **230** (19), 7093 – 7114.
- ROSSINELLI, D., HEJAZIALHOSSEINI, B., VAN REES, W. M., GAZZOLA, M., BERGDORF, M. & KOUMOUTSAKOS, P. 2015 MRAG-I2D: Multi-resolution adapted grids for remeshed vortex methods on multicore architectures. *Journal of Computational Physics* **288**, 1–18.